https://doi.org/10.1595/205651322X16595441894422 *Johnson Matthey Technol. Rev.*, 2023, **67**, (1), 36–46

JOHNSON MATTHEY
TECHNOLOGY REVIEW

technology.matthey.com

X-Ray Computed Tomography for Failure Mechanism Characterisation within Layered Pouch Cells: Part I

Lithium-ion battery safety

Drasti Patel, Hamish Reid
Electrochemical Innovation Lab, Department of Chemical Engineering, University College London, Torrington Place, London, WC1E 7JE, UK

Sarah Ball[$]**
Johnson Matthey, 142A Park Drive, Milton Park, Abingdon, OX14 4SE, UK

Dan J. L. Brett, Paul R. Shearing*
Electrochemical Innovation Lab, Department of Chemical Engineering, University College London, Torrington Place, London, WC1E 7JE, UK; The Faraday Institution, Quad One, Becquerel Avenue, Harwell Campus, Didcot, OX11 0RA, UK

Email: *p.shearing@ucl.ac.uk;
**sarah.ball@evmetalsgroup.co.uk

[$]Present address: EV Metals UK Ltd, 142A Park Drive, Milton Park, Abingdon, Oxfordshire, OX14 4SE, UK

PEER REVIEWED

Submitted 28th February 2022; Revised 8th July 2022; Accepted 2nd August 2022; Online 3rd August 2022

The assessment of lithium-ion battery (LIB) safety is a multiscale challenge: from the whole-cell architecture to its composite internal three-dimensional (3D) microstructures. Substantial research is required to standardise failure assessments and optimise cell designs to reduce the risks of LIB failure. In this two-part work, the failure response of a 1 Ah layered pouch cell with a commercially available nickel manganese cobalt (NMC) cathode and graphite anode at 100% state of charge (SOC) (4.2 V) is investigated. The mechanisms of two abuse methods: mechanical (by nail penetration) and thermal (by accelerating rate calorimetry) are compared by using a suite of post-mortem analysis methods.

1. Introduction

1.1 Lithium-Ion Battery Failure

LIB is a key technology for the future of energy storage. Its high power, long cycle life and high specific energy alongside its decreasing manufacturing cost make it the electrochemical technology of choice for sustainable mobility and renewable energy implementation (1, 2). Concerns regarding LIB safety, however, continue to be prevalent in their widespread application (3). During operation outside of their normal (or safe) operating window, LIBs can ignite and initiate fires or release toxic gases (4). Although statistically rare (5), some LIB failures are heavily publicised: firstly due to the speed at which they're becoming an ubiquitous technology in modern society, but also because of their unique failure behaviour in terms of initiation, spread and duration when compared to other fire hazards (6). An example of LIB safety in the media is a product recall by Sony, Japan, in 2006 of 9.6 million LIBs powering laptops of well-known computer manufacturers (7) that were deemed fire hazards due to faulty crimping and the introduction of microscopic metal contaminants during manufacture. Similarly, 10 years later, Samsung, South Korea, recalled 2.5 million Note 7 mobile phones (8) because of the use of thinner than normal separators and poor alignment of components (9). More recent headlines include fires within electric vehicles (EVs) such as several Tesla Model S cars (Tesla Inc, USA) between 2013–2021 (10, 11) and a Jaguar I-Pace (Jaguar

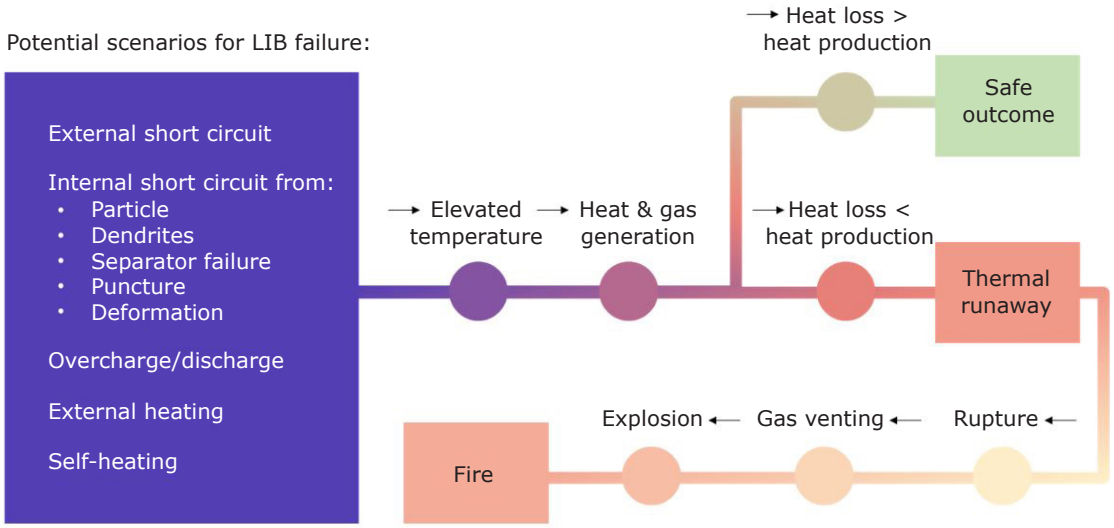

Fig. 1. Flowchart depicting the possible outcomes of a typical LIB failure sequence adapted from Total Battery Consulting (17)

Land Rover, UK) in 2021 (12). China, one of the world's largest markets for EVs reports sudden ignition due to contaminants and charging as the main causes of LIB fires in EVs (13). These events highlight the numerous variables that shape a battery safety incident; from the cause of failure, application type, and therefore battery format, management system and extent of the damage.

The mechanical integrity and heat dissipation of cells are important when considering LIB safety. The four most commonly used LIB formats are cylindrical, prismatic, coin, button or pouch. Prismatic cells generally have larger capacities than cylindrical, so fewer cells need to be connected in a pack for the desired capacity. Coin or button cells are small and typically used for laboratory-scale materials testing. Pouch cells offer greater flexibility in terms of matching the cell to a specific device shape (14). Within all of these formats, aside from the highly oxidising and reducing electrode materials (anode and cathode), the likelihood of failure and severity of an event is compounded by poor heat dissipation (3). The higher capacities of prismatic cells make it more difficult to dissipate heat (15) and make cooling more challenging, while the smaller physical size of cylindrical cells makes it easier to assemble them into packs (with gaps between cells) to improve overall heat dissipation. Prismatic and cylindrical cells have metallic outer shell casings that can withstand high pressure, whereas pouch cells are cased in aluminium-plastic composite films which make them more susceptible to deformations such as piercing, bulging or swelling. Furthermore, LIBs are composite systems made up of active particles, liquid electrolytes, metallic current collectors and separators, all of which should be addressed at each scale when assessing battery safety (3, 16).

Figure 1 illustrates the possible scenarios and outcomes of LIB failure. In cases where heat generation is not controlled, elevated temperatures may trigger a series of undesirable exothermic reactions that could sustain themselves enough to cause ruptures, venting of gases, explosions and eventually lead to fires (i.e. thermal runaway). The response of a LIB in situations where mechanical damage to shell casings (punctures or compression), electrical (overcharge/discharge or short circuit) or thermal damage (local heating) has occurred will vary depending on the format of the cell and its integrated battery management system (BMS), its capacity and its chemistry (18). Therefore, an effective strategy to interpret LIB safety and reduce the number of failure events is to characterise features across these multiple scales: from the whole-cell architecture to its individual components.

1.2 Investigation of Lithium-Ion Battery Safety

Manufacturers, organisations and battery researchers investigate and characterise the various mechanisms related to LIB safety by deliberately creating scenarios that may trigger thermal runaway. A test setup can involve overcharge/discharge, heating, short

Table I Summary of Heating and Nail Penetration Testing Guidelines from Five Selected Safety Testing Standards (16)

Trigger mechanism for battery failure	Safety testing standard				
	GB/T 31485-2015	IEC62133	SAE J2464	VW PV8450	USABC-GM
Heating	Heating at 5°C min^{-1} from 25°C to 130°C, hold for 30 min	130°C, 10 min	Maximum stable temperature	2°C min^{-1} to 130°C or 200°C hold for 30 min	0.5°C min, 50–150°C, hold for 30 min
Nail penetration	Penetration rate: 25 mm s^{-1}, diameter: 5–8 mm, 100% depth	n/a	80 mm s^{-1}, diameter: 3 mm, 100% depth	0.1 mm s^{-1}, diameter: 1 mm stainless steel, 2 mm depth	80 mm s^{-1}, diameter: 3 mm, 100% depth

circuit, internal short circuit, nail penetration or crushing. Despite standardisation efforts across these, current LIB safety testing standards have different guidelines for each. **Table I** summarises two methods (heating and nail penetration) used to trigger battery failure in five selected safety testing standards adapted from Chen *et al.* (16).

Heating tests are used to analyse the LIBs' thermal stability and heat distribution. GB/T 31485-2015 (19) deems a battery as 'safe' if it does not leak or combust after it is placed in a hot box and heated to 130°C at 5°C min^{-1} and kept at this temperature for 30 min. Nail penetration tests are designed to simulate an internal short circuit that may occur when the internal components are penetrated with impurities. An internal short circuit event generates large quantities of local heat which may lead to thermal runaway. According to GB/T 31485-2015, the battery should be at 100% SOC before it is penetrated by a high-temperature resistant stainless-steel nail (with a diameter between 5–8 mm) at a speed of 25 mm s^{-1}. The penetration position should also be as close to the geometrical centre of the cell and the nail should reach 100% of the depth of the battery.

Several research efforts have been made to compare the results of varying the battery SOC and capacity when heating as well as the depth and position of the nail during penetration tests. For example, Mendoza-Hernandez *et al*. report that thermal runaway is triggered much sooner and at a lower onset temperature in a cell at 100% SOC compared to 50% SOC (20). The severity of reactions is reported to be greater when a cylindrical cell is penetrated at the centre as opposed to the top and bottom, while higher nail penetration speeds decreased the uniformity of temperature distribution within the cell (21). Therefore, it is crucial to consider how such variations can affect the extent of failure and interpretation of LIB safety.

1.3 Thermal Analysis

In a comprehensive review of LIB fire safety studies, Ruiz *et al*. report that most literature focuses on single cell and component scales as opposed to module or pack scales (22). The failure behaviour of larger scale battery packs is different to individual cells and so the outcome of investigations also differs depending on the scale at which they are studied. Investigations can therefore be categorised by order of 'layer of protection' starting from prevention, compartmentation and detection to suppression of the fire (22). The prevention layer aims to avoid the failure scenario altogether and is the category for most single cell and component scale investigations. For this, the fundamental mechanisms that trigger and sustain the failure need to be understood; which is also where the focus of the current work lies.

Many studies have analysed the behaviour of LIBs at elevated temperatures and a set of key characteristic reactions during failure have been established (23). Adiabatic calorimetry (for example accelerating rate calorimetry (ARC) and differential scanning calorimetry (DSC)) have been used to investigate the decomposition of materials as individual components as well as components within a complete cell (24–27). It is generally known that once initiated (by a high temperature), a series of exothermic reactions will begin. First is the decomposition of the solid electrolyte interphase (SEI) layer typically between 60–100°C (18). This is a thin passivating layer that forms across the electrode layer surface and its decomposition generates gas and leaves the active electrode surface exposed to

electrolyte. Intercalated lithium on the anode reacts with the electrolyte and further heat and gas is generated. As the temperature of the cell increases, the cathode layer becomes unstable and begins to decompose (28). Furthermore, the overpressure within the cell may cause the outer casing of the cell to break or rupture. The introduction of oxygen to the system creates a flammable mixture and combustion reactions may follow (causing flames and fires) (29).

This reaction series and its associated kinetic parameters has been extensively modelled to understand and predict thermal runaway (30–32). The effects of cell geometry and configuration were studied by Lopez *et al*. who found that a prismatic shape had a slower temperature response and failure reaction kinetics than a cylindrical shape (33). Several models exist for thermal runaway triggered by various mechanical loadings and crash events; however, Zhu *et al*. concludes that due to the inhomogeneity between the numerous behaviours such as temperature, pressure-dependence, anisotropy or ductile fracture, each component (current collector, coating, separator, shell casing) exhibits, models are currently limited to the microscale (34).

1.4 Image Analysis

When attempting to understand the evolution of a particular failure mechanism within a LIB, it is important to consider the method by which the failed batteries are examined. Waldmann *et al*. reviews state-of-art methods by which aged cells are disassembled including microscopy, various chemical methods which are sensitive to electrode surfaces and reconstruction of electrodes into half and full cells (35). However, each method only observes a specific aspect of a LIB material behaviour making it difficult to characterise failure mechanisms using only electrochemical and physicochemical measurements of single materials (36). Imaging techniques such as scanning electron microscopy (SEM) (37), X-ray radiography (38–40), X-ray computed tomography (CT) (41–43) and neutron tomography (44) have been proven to be useful complementary methods to obtain visual observations of materials during and after a failure incident.

Mao *et al*. compare the anode extracted from a cylindrically wound cell after nail penetration with that of a pristine graphite anode and finds that the layered structure is still intact but has some additional fragments and voids where flammable materials may have been consumed by the thermal runaway reactions (21). Micro-CT was used in combination with X-ray diffraction (XRD) by Zhang *et al*. to visualise the cross-section of a jelly-roll pouch cell. A buckling behaviour was observed at the folded edges of the electrode layers as a function of extreme cycling. Ripples created by this posed a high chance of internal short circuits. As a result, the authors proposed optimised anode layer structures that controlled the distribution of stress and constraint in a jelly-roll cell (45).

The impact of low-temperature charging on the degradation of LIB materials was conducted by We *et al*. using a cell-opening method where the jelly-roll structure was unwound and separated into cathode, anode and separator. They were visually inspected for surface smoothness, detachment of active material and regions of exfoliation from the current collectors. Lithium plating on the anode was observed, and later SEM scans revealed cracks between primary particles when compared with fresh cell materials (46).

Finegan *et al*. investigated the effects of overcharge-induced thermal runaway on LIB materials using *operando* X-ray CT. A post-mortem multiscale approach was introduced whereby significant morphological and phase changes in a $LiCoO_2$ pouch cell after failure were examined using X-ray CT at the whole cell, bulk electrode structure and particle scales. The post-mortem battery architecture, bulk electrode and particle degradation revealed how failure mechanisms propagated across multiple spatial resolutions (47).

As demonstrated by literature, X-ray CT for post-failure analysis is predominantly used to see where failure-causing defects are located (48) and to assess where samples should be extracted from upon cell opening for further analysis (36). However, X-ray CT offers a wide range of imaging capabilities across multiple length scales that are often scattered in their application or approach and largely underused when characterising LIB failure. This work aims to combine some of the existing X-ray CT imaging methods for battery materials and introduces a step-by-step procedure for post-failure analysis of LIBs that involves whole-cell imaging, cell-opening and material extraction. Furthermore, the results obtained from sample preparation techniques that are non-invasive and invasive are compared regarding representativeness. Investigations are carried out for two different failure triggers (a thermally failed and a nail penetrated cell) which provide a range of characteristic failure features such as swelling, rupture or cracking. As a result, the whole-cell

architecture and electrode deformations can be compared against a pristine cell and for each failure mechanism. Additionally, the failure mechanisms are discussed from a failure prevention perspective, i.e. finding the mechanisms by which Joule heating or material decomposition occurs and how they can be mitigated: by controlling heat generation and enhancing heat dissipation within a pouch cell. This work addresses the challenge of consistency across existing LIB failure characterisation. Overall, the benefits of X-ray CT to aid the design, manufacture and use of LIBs in ways that can mitigate known safety hazards are demonstrated.

2. Experimental

This study combined battery failure testing with imaging to develop a guide for post-failure LIB analysis. The method followed a step-by-step investigation where failed cells were initially inspected as a whole, by eye and using X-ray CT for large characteristic features such as pouch swelling and later opened to extract materials for investigations using micro- and nanoscale X-ray CT. Investigations at smaller length scales provided an insight into the effects of battery failure on bulk and individual particles. Features such as particle cracking and the extent to which contaminants penetrated the electrode layer particles could be determined. Three 1 Ah layered lithium-ion batteries with a pouch cell format were tested for their response to two battery failure trigger modes. One cell was assigned as the control (Cell 1), and the remaining cells were investigated under external heating (Cell 2) and nail penetration (Cell 3), respectively. Details of the failure methods and measurements are described in Section 2.2. All cell samples consisted of 21 double-sided electrode layers, with 10 positive electrodes, denoted as the cathode, and 11 negative electrodes (graphite) denoted as the anode. The cathode material, lithium nickel manganese cobalt oxide (NMC811), was sourced from Targray, Canada. The electrochemical properties and assigned failure modes for each cell are summarised in **Table II**.

2.1 Cell Fabrication and Electrochemical Characterisation

The electrode processing, drying and cell assembly were all carried out at QinetiQ Group Plc, UK, on behalf of Johnson Matthey using commercially available materials. The cells were assembled inside a dry room with a –40°C dew point. For fabrication of pouch cells, electrodes with 36.5 × 49.0 mm dimension (electrode area = 17.885 cm^2) with an additional uncoated tab area were punched from laminated double-sided sheets. Pouch cells were assembled with 10 cathode and 11 anode layers, giving a total active area of 357.7 cm^2. The cathode was deposited on an aluminium current collector with a thickness of 15 µm and the anode was deposited on a copper current collector with a thickness of 10 µm.

The electrochemical performance of the pouch cells was tested in a two-electrode configuration using either a VMP3 Multichannel Potentiostat (BioLogic, France) or MSTAT 8000 (Arbin Instruments, USA) battery cycler. The cells underwent a constant-current constant-voltage (CCCV) formation protocol with three cycles between 2.7 V and 4.2 C using a C-rate of C 10^{-1} at 21°C. A current cut-off of 0.05 C was used for the constant voltage step. The specific capacity and current density were measured with respect to the mass of the active material.

2.2 Battery Failure Methods and Measurements

2.2.1 Thermal: External Heating by Accelerating Rate Calorimetry

ARC was used to determine the onset temperature for thermal runaway and the rate of heat generation

Table II Summary of Samples, Electrochemical Properties and Assigned Failure Modes

Sample code	Anode nominal capacity, Ah	Cathode nominal capacity, Ah	Ratio Q_{an}/Q_{cath} per 4.3 V	Specific capacity, mAh g^{-1}	Specific energy, Wh kg^{-1}	Cell failure mode
Cell 1	1.418	1.206	1.16	193.7	215.0	Pristine cell (no failure mode)
Cell 2	1.426	1.215	1.16	195.7	218.2	External heating by ARC
Cell 3	1.438	1.215	1.17	194.7	216.7	Internal short circuit by nail penetration

within Cell 2 during failure. The pouch cell was cycled by a CCCV protocol conducted at 1 C constant current, from 3.0–4.2 V, and using a constant voltage protocol until the current cut-off of 0.05 C. Before conducting the ARC experiments, the open circuit voltage was checked to ensure no voltage drop had occurred. The cell was heated up using ARC inside an adiabatic chamber (Phi-TEC battery test calorimeter, H.E.L Group, UK) with a heat-wait-search (HWS) protocol. Two thermocouples were attached to the bottom and top of the cell as close to the centre as possible. A heating coil was wound around the sample and secured using aluminium tape and the thermocouples were secured using glass fibre tape. A photograph of the cell setup inside the calorimeter is shown in Figure S1 in the Supplementary Information. Once the cell had reached a start temperature of 50°C, HWS was initiated. After which, the calorimeter increased the temperature in discrete steps of 5°C and monitored the cell temperature for 5 min. If in this time the temperature remained unchanged, up to a threshold value, approximately 0.02°C min^{-1}, the calorimeter then continued to increase the temperature by 5°C until self-heating was detected (41).

2.2.2 Mechanical: Internal Short Circuit by Nail Penetration

The nail penetration test on Cell 3 was conducted using a battery penetration instrument (MSK-800-TE9002 pneumatic nail penetration tester, MTI Corporation, USA). The instrument is a large fire-proof chamber fitted with an air vent, clamps to hold the sample in place and a stainless-steel nail with a 4 mm diameter. The pouch cell was fully charged to the maximum rated voltage, 4.2 V at 1 C using a CCCV charging protocol and was mounted horizontally. The nail was positioned so it would penetrate the centre of the cell and the penetration depth was chosen to fully pierce through all the layers at a speed of approximately 30 mm s^{-1}. After penetration, the nail was slowly reversed out of the cell. Heat and voltage measurements were not recorded for this cell during failure. The behaviour of the cell was monitored by video and is available in Supplementary Information with the online version of this article.

2.3 Imaging

Tomographic reconstructions of multiple samples were produced using three laboratory-based X-ray CT systems: Nikon XT H 225 (Nikon Metrology, Japan), ZEISS Xradia 520 Versa (ZEISS, Germany) and ZEISS Xradia Ultra 810. Whole battery scans, (i.e. without cell disassembly) are defined as 'non-invasive' and battery component scans, for imaging bulk electrode layers and particles, are defined as 'invasive'. For the latter, the battery was carefully dismantled and photographed during each stage of disassembly for sample collection. Sample preparation methods for invasive X-ray CT scans are outlined in Section 2.4. The features of interest, spatial resolution and imaging instrument used are categorised by the sample preparation method (invasive or non-invasive) and shown in **Figure 2**.

For whole cell and region-of-interest (ROI), non-invasive scans, images were obtained using the Nikon XT H 225 (Nikon) and the ZEISS Xradia 520 Versa (ZEISS) with a 4 x objective lens, respectively. For the Nikon, an accelerating voltage of 210 kV was used with a tungsten target to generate 3176 projections for each of the datasets acquired. The datasets were subsequently reconstructed using CT Pro 3D software with a built-in filtered back projection algorithm. The acquired datasets had voxel sizes ranging from 27.8–33.6 µm. For the ROI datasets, a pixel binning of 1 was used and the voltage, exposure times, and number of projections were all varied for the sample type. The acquired pixel sizes are summarised in Table S1 in the Supplementary Information.

After opening the failed cells, samples were prepared according to the feature of interest as outlined in Section 2.4. The bulk electrode layer datasets were obtained using the ZEISS Xradia 520 Versa with a 40 x objective lens. Datasets for the thermally failed (Cell 2) and nail penetrated (Cell 3) cathode samples were obtained using a pixel binning of 2, a voltage of 80 kV and an exposure time of 5 s, while the anode datasets were obtained using a lower voltage at 60 kV while all other parameters remained the same. The acquired pixel sizes are summarised in Table S1 in the Supplementary Information.

High resolution images of the cathodes extracted from all three cells were obtained using the ZEISS Xradia Ultra 810 with a fixed energy 5.4 keV, quasi-monochromatic beam. A voxel size of 0.0631 µm was achieved for the pristine cathode and 0.126 µm for the post failure cathode samples.

All SEM micrographs were obtained using the ZEISS EVO 10 SEM instrument. An SE1 signal was used at a 15 kV accelerating voltage and approximate magnifications ranging from

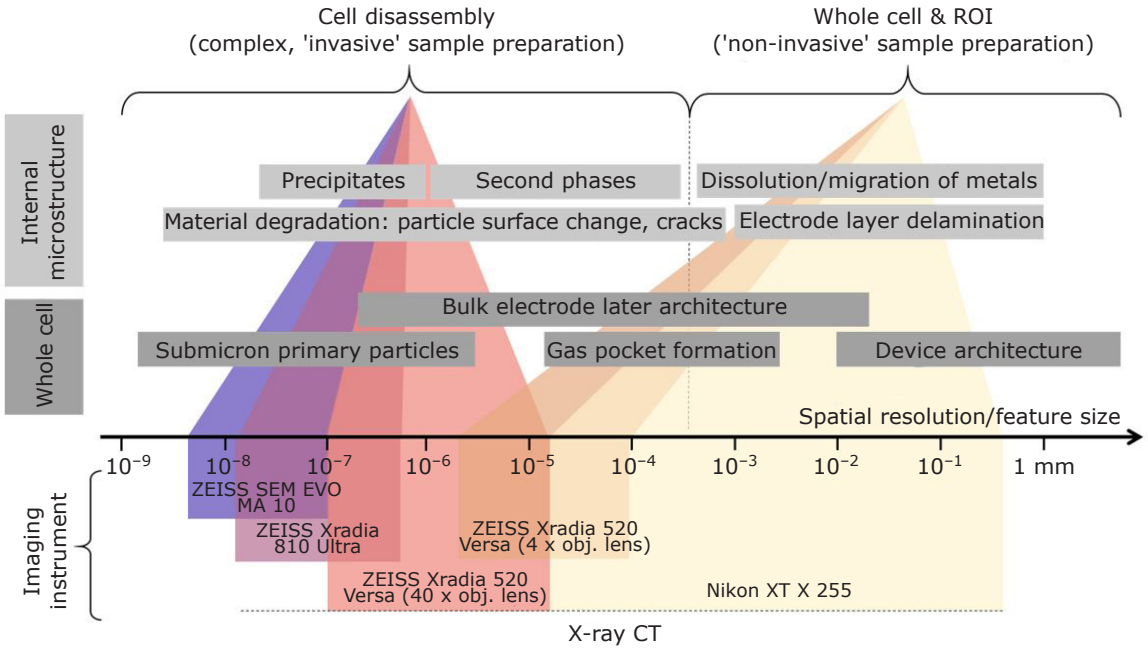

Fig. 2. Imaging instruments (SEM and X-ray CT) grouped for the type of sample preparation (invasive and non-invasive) required for the feature of interest/spatial resolution (adapted from Salvo *et al*. (49))

3300–8500, yielding pixel sizes between 35–90 nm for all images.

2.3.1 Image Processing

Reconstructed X-ray CT data was visualised using Avizo Fire 9.2 software (FEI Visualization Sciences Group, USA). For all datasets, a non-local means filter was applied to reduce noise and preserve phase boundaries. This procedure was performed to prepare the datasets for threshold-based binarisation. Phases were separated based on their greyscale values where weakly attenuating materials are displayed in shades of grey (such as the separator, graphite anode and aluminium current collector) and highly attenuating materials (such as the cathode active material and copper current collector) in white. Voxels in the bulk electrode layer and particle scans were assigned to a particle or pore phase based on the measured grayscale value. The resulting binary images were used for measurements of porosity and particle size distribution using the Avizo Fire 9.2 label analysis tool. Tortuosity factors and representative volume analyses were extracted using TauFactor, an open-source MATLAB® plugin, details of which are described in (50).

2.4 Post-Mortem Sample Preparation

Two methods were used to prepare the samples for the battery component (bulk electrode layer and particle morphology) analysis. Cells were left overnight in their respective instruments after failure for gases to safely dissipate. Once the cells had cooled to room temperature, they were imaged first *via* X-ray CT for the whole cell and ROI analysis. The cells were stored in air and later taken apart inside of a fume hood. For both cells, a scalpel was used to create an incision lengthwise at the side of the cell where the pouch had been vacuum sealed. The outer casing of the pouch was peeled away carefully without disrupting the electrode layers as shown in **Figure 3(a)** and **3(b)**. The electrode layer stack was removed first from within the cell casing by cutting the anode and cathode tabs. For the thermally failed cell (Cell 2), the central anode and cathode layers were removed and a 1 cm x 1 cm square from the centre of the electrodes was removed for further preparation (as shown in **Figure 3(a)** and **3(b)**). For the nail penetrated cell (Cell 3), the central anode and cathode layers were removed, and the separator was carefully peeled off their surfaces. 1 cm x 1 cm squares were cut from the centre of both electrodes of this cell and subsequently used for two-dimensional (2D) imaging *via* SEM. For 3D imaging *via* X-ray CT, the samples were processed further using a high precision laser, details of which follow.

Samples intended for 3D images of the bulk electrode were prepared by cutting 0.4 mm by 0.4 mm squares which were mounted onto a 3D printed stacker using Kapton tape. The samples

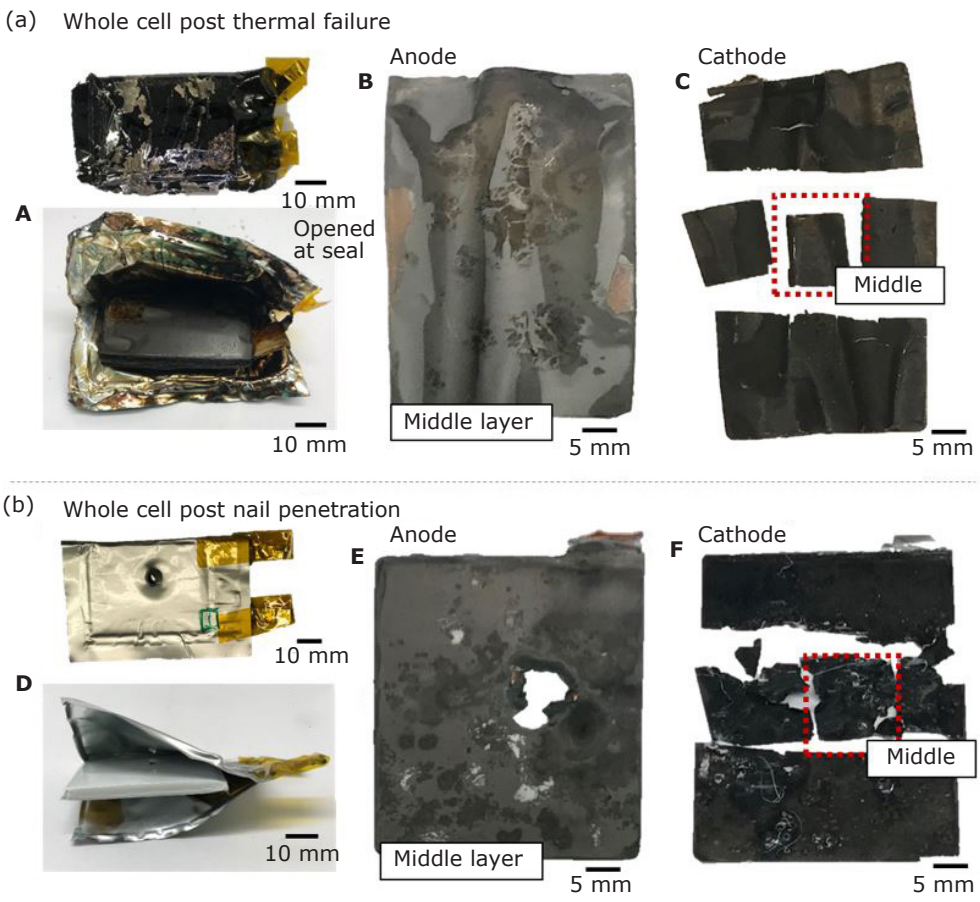

Fig. 3. Photographs showing the disassembly of: (a) the thermally failed cell (Cell 2); and (b) the nail penetrated cell (Cell 3). The aluminium-plastic composite casing was carefully cut at the vacuum sealed edge and peeled away in **A** and **D**. The central anode layer is shown in **B** and **E** and the central cathode layer is shown in **C** and **F** as well as where the samples for SEM and X-ray CT were extracted from

fitted within the field-of-view (FOV) of the 40 x objective lens, *ca*. 400 µm, in the X-ray micro-CT instrument (Zeiss Xradia 520 Versa) and were held upright in a 3D printed stacker (Figure S2 in the Supplementary Information) to reduce the overall signal-to-noise ratio and scan time. This method produced 3D images with a 0.387 µm voxel size of the four bulk electrode layers (anode and cathode each after thermal failure and nail penetration).

Samples intended for imaging at nanoscale resolutions to resolve individual particles (using the Zeiss Xradia Ultra 810) were prepared using a laser lathing micromachining technique (A Series Compact Laser Micromachining Tool, 532 nm wavelength, Oxford Lasers, UK) as described by Bailey *et al*. (51). Small disks of 1 mm diameter were cut from the bulk electrode layers, glued to a pin and milled down to a diameter <65 µm. All samples were imaged in the large field of view absorption mode with a 65 µm FOV.

3. Results and Discussion

Three proprietary pouch cell LIBs were investigated under two trigger mechanisms for failure: thermal by external heating and mechanical by nail penetration. Temperature measurements taken of the thermally failed cell (Cell 2) and a video recorded during the nail penetration test on Cell 3 reveal the behaviours of each cell during failure. A subsequent post-mortem analysis investigated the responses of the cells in the context of architectural changes to the cell structure as a whole, the microstructure of the bulk electrode layers (anode and cathode) and the particle morphologies (cathode). **Figure 3(a)** and **3(b)** show photographs of the whole cell after both types of tests. Upon initial inspection, the outer casing of the thermally failed cell (Cell 2) was significantly charred, and the cell was swollen with no visible ruptures. The nail penetrated cell (Cell 3) had a rupture through the cell as a result of the depth of penetration (100%). The separator remained intact for Cell 3 suggesting that it did not reach temperatures above 120°C, while the separator in the thermally failed cell had melted when temperatures reached >120°C. On disassembly of the cell, the copper current collector of the anode in the nail penetrated cell appeared brittle and the tab had detached from the bulk electrode layer stack. A comprehensive

investigation of a post-mortem analysis using X-ray CT and SEM techniques follows in Part (II) (52).

Acknowledgements

This work was supported by the Engineering and Physical Sciences Research Council (EPSRC), UK (EP/N032888/1, EP/R020973/1, EP/K005030/1, EP/M028100/1). Drasti Patel acknowledges funding from the EPSRC CASE Award scheme with Johnson Matthey. Paul Shearing acknowledges the support of The Royal Academy of Engineering (CiET1718/59) and The Faraday Institution (EP/S003053/1), grant number FIRG025 and FIRG028.

References

1. G. E. Blomgren, *J. Electrochem. Soc.*, 2017, **164**, (1), A5019
2. N. Nitta, F. Wu, J. T. Lee and G. Yushin, *Mater. Today*, 2015, **18**, (5), 252
3. D. H. Doughty and E. P. Roth, *Electrochem. Soc. Interface*, 2012, **21**, (2), 37
4. P. G. Balakrishnan, R. Ramesh and T. Prem Kumar, *J. Power Sources*, 2006, **155**, (2), 401
5. M. Jacoby, 'Assessing the Safety of Lithium-Ion Batteries', Chemical & Engineering News, Washington, DC, USA, 11th February, 2013
6. L. Bravo Diaz, X. He, Z. Hu, F. Restuccia, M. Marinescu, J. V. Barreras, Y. Patel, G. Offer and G. Rein, *J. Electrochem. Soc.*, 2020, **167**, 090559
7. G. Madway, K. Hamada, M. Negishi and K. Takenaka, 'Sony Recalls PC Batteries', ed. R. Joyce, Reuters, London, UK, 31st October, 2008
8. S. Y. Lee, 'Note 7 Fiasco Could Burn a $17 Billion Hole in Samsung Accounts', Reuters, London, UK, 11th October, 2016
9. M. J. Loveridge, G. Remy, N. Kourra, R. Genieser, A. Barai, M. J. Lain, Y. Guo, M. Amor-Segan, M. A. Williams, T. Amietszajew, M. Ellis, R. Bhagat and D. Greenwood, *Batteries*, 2018, **4**, (1), 3
10. E. Musk, 'Model S Fire', Tesla, Austin, USA, 4th October, 2013
11. H. Jin and D. Shepardson, 'Tesla Top-of-Range Car Caught Fire while Owner was Driving, Lawyer Says', ed. C. Cushing, Reuters, London, UK, 2nd July, 2021
12. A. Nedelea, 'Jaguar I-Pace Catches Fire while Charging in Hungary', InsideEVs, Miami, USA, 29th October, 2021
13. K. Koshika, 'Statistics and Analysis on Fire Accidents for EVs: China', EVS 16th Session, Gothenburg, Sweden, 11th–13th September, 2018, Vehicle Regulations Informal Working Groups, UNECE Transport Division, Geneva, Switzerland, 2018
14. G. Fisher, 'Pouch, Cylindrical or Prismatic: Which Battery Format will Rule the Market?', Addionics, London, UK, 14th April, 2021
15. J. Lamb, C. J. Orendorff, L. A. M. Steele and S. W. Spangler, *J. Power Sources*, 2015, **283**, 517
16. Y. Chen, Y. Kang, Y. Zhao, L. Wang, J. Liu, Y. Li, Z. Liang, X. He, X. Li, N. Tavajohi and B. Li, *J. Energy Chem.*, 2021, **59**, 83
17. D. Doughty, "Li Ion Battery Safety and Abuse Tolerance Report: A Systematic Account of Why Battery Safety Incidents Occur and How to Avoid Them", Total Battery Consulting, Petaluma, USA, 2017
18. X. Feng, M. Ouyang, X. Liu, L. Lu, Y. Xia and X. He, *Energy Storage Mater.*, 2018, **10**, 246
19. 'Safety Requirements and Test Methods for Traction Battery of Electric Vehicle', GB/T 31485-2015, General Administration of Quality Supervision Inspection and Quarantine of the People's Republic of China (AQSIQ), Beijing, China, 2015
20. O. S. Mendoza-Hernandez, H. Ishikawa, Y. Nishikawa, Y. Maruyama and M. Umeda, *J. Power Sources*, 2015, **280**, 499
21. B. Mao, H. Chen, Z. Cui, T. Wu and Q. Wang, *Int. J. Heat Mass Transfer*, 2018, **122,** 1103
22. V. Ruiz, A. Pfrang, A. Kriston, N. Omar, P. Van den Bossche and L. Boon-Brett, *Renew. Sustain. Energy Rev.*, 2018, **81**, (1), 1427
23. R. Spotnitz and J. Franklin, *J. Power Sources*, 2003, **113**, (1), 81
24. H. Maleki, G. Deng, A. Anani and J. Howard, *J. Electrochem. Soc.*, 1999, **146**, (9), 3224
25. E. P. Roth and D. H. Doughty, *J. Power Sources*, 2004, **128**, (2), 308
26. P. J. Bugryniec, J. N. Davidson, D. J. Cumming and S. F. Brown, *J. Power Sources*, 2019, **414**, 557
27. W.-C. Chen, Y.-W. Wang and C.-M. Shu, *J. Power Sources*, 2016, **318**, 200
28. X. Feng, M. Fang, X. He, M. Ouyang, L. Lu, H. Wang and M. Zhang, *J. Power Sources*, 2014, **255**, 294
29. Q. Wang, B. Mao, S. I. Stoliarov and J. Sun, *Prog. Energy Combust. Sci.*, 2019, **73**, 95
30. T. D. Hatchard, D. D. MacNeil, A. Basu and J. R. Dahn, *J. Electrochem. Soc.*, 2001, **148**, (7), A755
31. G.-H. Kim, A. Pesaran and R. Spotnitz, *J. Power Sources*, 2007, **170**, (2), 476
32. D. Ren, X. Liu, X. Feng, L. Lu, M. Ouyang, J. Li and X. He, *Appl. Energy*, 2018, **228**, 633
33. C. F. Lopez, J. A. Jeevarajan and P. P. Mukherjee, *J. Electrochem. Soc.*, 2015, **162**, (10), A2163
34. J. Zhu, T. Wierzbicki and W. Li, *J. Power Sources*, 2018, **378**, 153
35. T. Waldmann, A. Iturrondobeitia, M. Kasper, N. Ghanbari, F. Aguesse, E. Bekaert, L. Daniel, S. Genies, I. Jiménez Gordon, M. W. Löble, E. De

Vito and M. Wohlfahrt-Mehrens, *J. Electrochem. Soc.*, 2016, **163**, (10), A2149

36. C. J. Mikolajczak, T. Hayes, M. V Megerle and M. Wu, 'A Scientific Methodology for Investigation of a Lithium Ion Battery Failure', 2007 IEEE International Conference on Portable Information Devices, Orlando, Florida, USA, 25th–29th May, 2007, IEEE, Piscataway, USA, 6 pp
37. N. Williard, B. Sood, M. Osterman and M. Pecht, *J. Mater. Sci.: Mater. Electron.*, 2011, **22**, (10), 1616
38. D. P. Finegan, M. Scheel, J. B. Robinson, B. Tjaden, I. Hunt, T. J. Mason, J. Millichamp, M. Di Michiel, G. J. Offer, G. Hinds, D. J. L. Brett and P. R. Shearing, *Nat. Commun.*, 2015, **6**, 6924
39. D. P. Finegan, E. Darcy, M. Keyser, B. Tjaden, T. M. M. Heenan, R. Jervis, J. J. Bailey, R. Malik, N. T. Vo, O. V. Magdysyuk, R. Atwood, M. Drakopoulos, M. DiMichiel, A. Rack, G. Hinds, D. J. L. Brett and P. R. Shearing, *Energy Environ. Sci.*, 2017, **10**, (6), 1377
40. D. P. Finegan, B. Tjaden, T. M. M. Heenan, R. Jervis, M. Di Michiel, A. Rack, G. Hinds, D. J. L. Brett and P. R. Shearing, *J. Electrochem. Soc*, 2017, **164**, (13), A3285
41. D. Patel, J. B. Robinson, S. Ball, D. J. L. Brett and P. R. Shearing, *J. Electrochem. Soc.*, 2020, **167**, (9), 090511
42. T. Yokoshima, D. Mukoyama, F. Maeda, T. Osaka, K. Takazawa, S. Egusa, S. Naoi, S. Ishikura and K. Yamamoto, *J. Power Sources*, 2018, **393**, 67
43. E. Sahraei, M. Kahn, J. Meier and T. Wierzbicki, *RSC Adv.*, 2015, **5**, (98), 80369
44. R. F. Ziesche, T. Arlt, D. P. Finegan, T. M. M. Heenan, A. Tengattini, D. Baum, N. Kardjilov, H. Markötter, I. Manke, W. Kockelmann, D. J. L. Brett and P. R. Shearing, *Nat. Commun.*, 2020, **11**, 777
45. N. Zhang and H. Tang, *J. Power Sources*, 2012, **218**, 52
46. W. Wu, R. Ma, J. Liu, M. Liu, W. Wang and Q. Wang, *Int. J. Heat Mass Transfer*, 2021, **170**, 121024
47. D. P. Finegan, M. Scheel, J. B. Robinson, B. Tjaden, M. Di Michiel, G. Hinds, D. J. L. Brett and P. R. Shearing, *Phys. Chem. Chem. Phys.*, 2016, **18**, (45), 30912
48. X.-Y. Yao and M. G. Pecht, *IEEE Access*, 2019, **7**, 24082
49. L. Salvo, M. Suéry, A. Marmottant, N. Limodin and D. Bernard, *Comptes Rendus Phys.*, 2010, **11**, (9–10), 641
50. S. J. Cooper, A. Bertei, P. R. Shearing, J. A. Kilner and N. P. Brandon, *SoftwareX*, 2016, **5**, 203
51. J. J. Bailey, T. M. M. Heenan, D. P. Finegan, X. Lu, S. R. Daemi, F. Iacoviello, N. R. Backeberg, O. O. Taiwo, D. J. L. Brett, A. Atkinson and P. R. Shearing, *J. Microsc.*, 2017, **267**, (3), 384
52. D. Patel, H. Reid, S. Ball, D. J. L. Brett and Paul R. Shearing, *Johnson Matthey Technol. Rev.*, 2023, **67**, (1), 47

The Authors

Drasti Patel is a PhD researcher at the Electrochemical Innovation Lab (EIL) at University College London (UCL), UK. Her project is part sponsored by Johnson Matthey. Her research interests are in lithium-ion battery materials characterisation and failure assessment using X-ray CT imaging and calorimetry.

Hamish Reid is currently a PhD researcher at the EIL at UCL. Prior to joining the EIL, Hamish gained a Chemistry with a Year in Industry MChem at the University of Sheffield, UK, where he spent a year working at The Dow Chemical Company, USA. After graduating, Hamish worked at Faradion Ltd, UK, researching cathode and anode materials for rechargeable sodium-ion batteries. His current research interests include X-ray imaging, battery safety and degradation of high nickel content lithium-ion cathode materials. Hamish's doctorate work is partly funded by Johnson Matthey.

At the time of writing, Sarah Ball was Applications Technology Manager at Johnson Matthey. She has experience managing technical projects for lithium-ion batteries and hydrogen fuel cells, focusing on testing, evaluation and improvement of cathode and anode materials.

Dan Brett is a professor of Chemical Engineering at UCL. His research interests lie in electrochemical energy conversion and storage, electrochemical sensors; electroanalysis, hybrid vehicles and microgeneration technologies. He is also active in modelling, instrumentation development, engineering design, device fabrication, materials development and technoeconomic analysis of electrochemical energy conversion technologies.

Paul Shearing is a professor of Chemical Engineering at UCL and Royal Academy Engineering Chair in Emerging Battery technologies. His research interests lies in the design of electrochemical processes in devices including fuel cells, batteries and electrochemical reactors. He is involved in a wide range of projects which includes the understanding and development of batteries, fuel cells and other electrochemical processes and leads the LiSTAR project and the SAFEBATT project on battery safety, under the auspices of The Faraday Institution, UK.